SCATTERING-BASED SENSITIVITY KERNELS FOR TIME-LAPSE DIFFERENTIAL-WAVEFORM INVERSION

D. Macedo, I. Vasconcelos and J. Schleicher

email: *dlmacbr@gmail.com*

keywords: *Full waveform inversion, Scattering theory,time-lapse seismic, multiple scattering*

ABSTRACT

Time-lapse seismic surveys are a powerful reservoir monitoring tool. The basic approach in time-lapse surveys is to image the changes in the reservoir by subtracting separated-in-time seismic images of the reservoir. Recently FWI has been used to improve time-lapse monitoring. However, in practice, nonlinear gradient-based FWI is limited due to its notorious sensitivity to the choice of the starting model. Kernel decomposition based on scattering theory allows to break the acoustic-wavefield sensitivity kernels with respect to model parameters into background and singular parts, which should help to address model-convergence issues in FWI. Here we apply scattering theory to the time-lapse problem, considering the time-lapse change as a perturbation of the singular part of the model. We make use of the time-lapse differential-waveform inversion framework, with the linearized scattering-based decomposition of the sensitivity kernel. Our numerical examples demonstrate that the inclusion of the singular part into the model used for backpropagation helps to improve the perturbation estimates from FWI by taking advantage of the additional subsurface illumination provided by multiple-scattering phenomena.

INTRODUCTION

Over the past few years, time-lapse seismic surveys has become a powerful tool used to monitor the fluid-flow in a producing reservoir. Generally speaking, such a survey consists in acquiring and analyzing multiple seismic data, repeated at the same site over time in order to look for differences from which one can infer the changes in the reservoir due to production. This is possible because, as fluid saturations and pressures in the reservoir change, the seismic reflection properties change accordingly.

A seismic image contains information on reflections that depends on both the geological structure and its fluid contents. On a single-time images these contributions are coupled and difficult to separate. The basic approach in time-lapse surveys is to image the changes in the reservoir by subtracting subsequent time-lapse seismic images of the reservoir from one another. Assuming that geology is time-invariant during production and that repeatability in the seismic data acquisition is, in some way, assured, the image difference from a time-lapse survey would indicate the changes due only to the fluid-flow since, to first order, the geology part subtracts out since it is time invariant (Lumley, 2001).

Recently, full waveform inversion (FWI) has been used as an alternative time-lapse monitoring tool (Queißer and Singh, 2013; Yang et al., 2011; Zheng et al., 2011). FWI allows the reconstruction of high-resolution velocity models of the subsurface through the extraction of the full information content of seismic data (Tarantola, 1984; Virieux and Operto, 2009). Since the FWI approach delivers high resolution quantitative images of macro-scale physical parameter, it ought to be a good candidate for monitoring applications to reconstruct the parameter variation through time evolution (Asnaashari et al., 2012).

Asnaashari et al. (2012) studied the robustness of three different FWI methods applied to time-lapse problems: differential method, parallel difference method and the sequential difference method. In the differential method, instead of minimizing the difference between the observed and modeled data, the

difference of the differential data between two sets of data is minimized to obtain the time-lapse change estimate (Watanabe et al., 2004). The parallel difference method considers independent inversion of the baseline and monitor data-sets, using a similar starting model (Plessix et al., 2010). The sequential difference method uses the recovered baseline model as a starting model for the monitor data inversion.

While in principle capable of handling all aspects of wave propagation affecting the seismic data, including full nonlinearity, in practice nonlinear gradient-based FWI is limited to localizing the nearest local mimimum, leading to its notorious sensitivity to the choice of the starting model. This is so because, for narrow-offset acquisition of reflection data, the seismic wavefield is rather insensitive to high/intermediate wavelengths.

In previous work, we sought to help addressing model convergence issues in FWI. For this purpose, we studied a wavefield decomposition based on scattering theory that allows to break the acoustic-wavefield sensitivity kernels (SKs) with respect to model parameters into background and singular parts (Macedo et al., 2011, 2012a,b, 2013). We were able to demonstrate that the forward kernel decomposition is successful in revealing subkernels that unravel different levels of non-linearity with respect to data and model. This, in turn, can be translated into different levels of interaction between non-, single-, and multiple-scattered information that otherwise would be hidden in the full-wavefield sensitivity kernels. Moreover, we predicted that part of the answer to the problem of lacking low-frequency information on the model should lie in utilizing scattered wavefields, because these travel through the medium long enough to carry this information (see also Snieder et al., 2002).

In this work we apply our scattering decomposition to the time-lapse problem, considering the time-lapse change as a perturbation of the singular part of the model, i.e., perturbation of the scattering potential. Under the differential-method framework, we demonstrate that the scattering-based decomposition of the sensitivity kernels allows to take advantage of the illumination of the time-lapse change due to multiple-scattering phenomena in order to improve the perturbation estimates from FWI.

SCATTERING-BASED SENSITIVITY KERNELS

The wavefield perturbation δp due to a medium change can be evaluated, under the assumptions of the Born approximation, using so-called secondary or adjoint sources (Tarantola, 1984). Based on scattering theory, Macedo et al. (2011) decompose the full-acoustic-wavefield perturbation δp into 13 components (one reference-wavefield perturbation δp_0 and 12 parts of the scattered-wavefield perturbation δp_s, see Figure 1) that reveal different levels of interaction between single and multiple-scattered information within data (see also Macedo et al., 2012a,b, 2013).

The reference-wavefield perturbation and all components of the scattered-wavefield perturbations have the same functional structure (time dependency is ommited for simplicity):

$$\delta p_0 \quad \text{or} \quad \delta p_{s,\alpha\mathcal{O}\gamma}(x_g;x_s) = \int_{\mathbb{V}} d^3x'\, G_\gamma(x';x_g) * \mathcal{L}_{\mathcal{O}}\left[p_\alpha(x';x_s)\right] \ , \tag{1}$$

where the subscripts α and γ denote the involved wavefield parts, with p_γ denoting the incoming source-

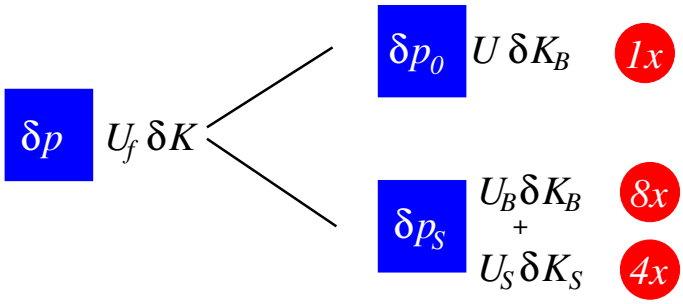

Figure 1: Subkernels obtained from the decomposition considering no perturbation in density. U_f, U, U_B and U_S are Frechet's derivatives, also called sensitivity kernels. The first is the full-wavefield derivative with respect to the full bulk modulus, the second is the reference-wavefield derivative with respect to the background bulk modulus. The last two are scattered-wavefield derivatives with respect to the background and singular part of the bulk modulus respectively.

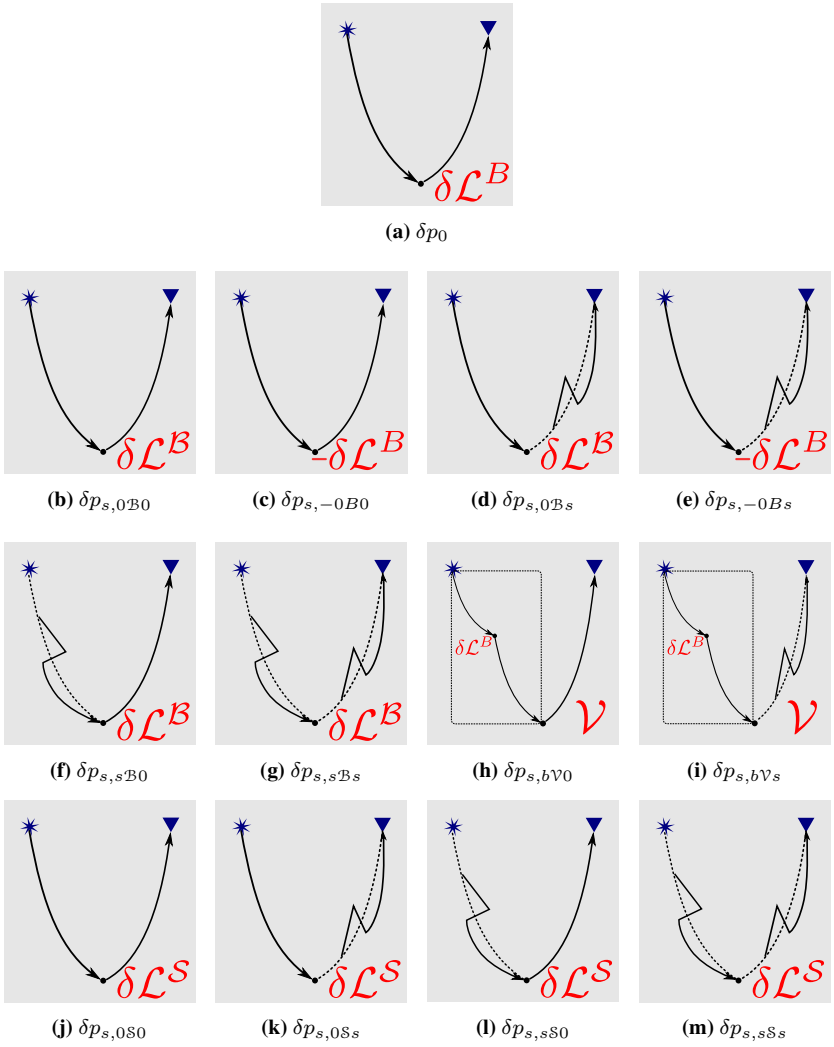

(a) δp_0 **(b)** $\delta p_{s,0\mathcal{B}0}$ **(c)** $\delta p_{s,-0B0}$ **(d)** $\delta p_{s,0\mathcal{B}s}$ **(e)** $\delta p_{s,-0Bs}$ **(f)** $\delta p_{s,s\mathcal{B}0}$ **(g)** $\delta p_{s,s\mathcal{B}s}$ **(h)** $\delta p_{s,b\mathcal{V}0}$ **(i)** $\delta p_{s,b\mathcal{V}s}$ **(j)** $\delta p_{s,0\mathcal{S}0}$ **(k)** $\delta p_{s,0\mathcal{S}s}$ **(l)** $\delta p_{s,s\mathcal{S}0}$ **(m)** $\delta p_{s,s\mathcal{S}s}$

Figure 2: Physical interpretation of the subkernel contributions. Each one of the cartoons shows three elements: *source-side wavefield*; the *operator* applied to generate the secondary source; and the *receiver-side wavefield extrapolator*. Subcaptions indicate the name of the contribution with subscripts explained in the text.

side wavefield and G_α the involved receiver-side Green's function extrapolator. Also, $\mathcal{L}_\mathcal{O}$ is a differential operator indicating the acting medium perturbation, and the asterisk ($*$) denotes time convolution.

Figure 2 illustrates the possible values that the subscripts α, $\mathcal{O}$ and γ in equation (1) can take. The receiver-side Green's function can either be the one for the reference wavefield, represented by subscript $\gamma = 0$, or the scattered part, represented by $\gamma = s$. The source wavefield can, in addition to the reference or scattered wavefield represented by $\alpha = 0$ or $\alpha = s$, respectively, also be the wavefield perturbation due to the background-medium perturbation, represented by $\alpha = b$. The operator $\mathcal{L}_\mathcal{O}$ represents the part of the medium that scatters the incoming wavefield, thus causing the secondary sources. The values B, $\mathcal{B}$, $\mathcal{S}$, and $\mathcal{V}$ for subscript $\mathcal{O}$ represent the background secondary potential, background part of the full secondary potential, singular part of the full secondary potential, and scattering potential, respectively. For details, please refer to Macedo et al. (2011, 2012b).

For simplicity, let us analyze the situation without density perturbation. Then, the expression to evaluate

the reference- and scattered-wavefield residual is given by

$$\begin{bmatrix} \widehat{\delta p}_0 \\ \widehat{\delta p}_s \end{bmatrix} = \begin{bmatrix} U & 0 \\ \sum_i U_{B,i} & \sum_j U_{S,j} \end{bmatrix} \begin{bmatrix} \delta K_B \\ \delta K_S \end{bmatrix}, \tag{2}$$

with $i = 0\mathcal{B}0$, $0\mathcal{B}s$, $s\mathcal{B}0$, $s\mathcal{B}s$, $-0B0$, $-0Bs$, $b\mathcal{V}0$, $b\mathcal{V}s$, and $j = 0\mathcal{S}0$, $0\mathcal{S}s$, $s\mathcal{S}0$, and $s\mathcal{S}s$.

Under the discussed separation into background and singular components, estimates of background and singular model perturbations can be evaluated separetely by backprojecting the residuals. The perturbation estimates are given by the adjoint of equation (2). They are obtained from

$$\begin{bmatrix} \delta K^{\text{est}}_{B,0} + \sum_i \delta K^{\text{est}}_{B,i} \\ \sum_j \delta K^{\text{est}}_{S,j} \end{bmatrix} = \begin{bmatrix} U^\dagger & \sum_i U^\dagger_{B,i} \\ 0 & \sum_j U^\dagger_{S,j} \end{bmatrix} \begin{bmatrix} \widehat{\delta p}_0 \\ \widehat{\delta p}_s \end{bmatrix}. \tag{3}$$

The explicit meaning of these expressions is analogous to the representation of the estimate in Tarantola (1984). At each point x of the model, each contribuition to the perturbation estimate is the cross-correlation between the direct wavefield from source with the (once or twice) backpropagated residual from the receivers. For example, estimate $\delta K^{\text{est}}_{B,0\mathcal{B}s}$ explicitly reads

$$\delta K^{\text{est}}_{B,0\mathcal{B}s}(x) = \sum_s \sum_g \int d\omega \, \frac{-\omega^2}{K^2(x)} \overbrace{\widehat{p}^\dagger_0(x,\omega;x_s)}^{\text{direct wavefield}} \underbrace{\widehat{G}^\dagger_0(x,\omega;x_g)\widehat{\delta p}_s(x_g,\omega;x_s)}_{\text{back-propagation of } \widehat{\delta p}_s} . \tag{4}$$

Proper substitution of the wavefields and potentials yields the corresponding explicit expressions for the other sensitivity kernels.

Time-lapse survey as a FWI scattering problem

To apply the above decomposition theory to a time-lapse survey, we think of the baseline model as decomposed into a background and a singular part. We consider both parts of the baseline model as known. The background part could be, for instance, the best smooth velocity model from a conventional inversion technique, and the singular part could be determined by the reflector positions in the corresponding migrated image. Then, the time-lapse changes can be considered as (unknown) perturbations to the singular and/or background parts.

The situation is the simplest, if we consider the time-lapse change as a perturbation of the singular part only. According to equation (2), the data difference between baseline and monitor is then the scattered-wavefield residual, and the model perturbation estimates are

$$\delta K^{\text{est}}_S = \sum_j \delta K^{\text{est}}_{S,j} = \sum_j U^\dagger_{S,j} \widehat{\delta p}_s, \tag{5}$$

where the sum consists only of the four terms associated with the singular part of the full secondary potential.

NUMERICAL EXPERIMENTS

To test our approach, we have set up two synthetic experiments with simple layered models (see Figure 3). The two baseline models are identical except for the velocity contrast at the deepest interface. In the first model, this interface is a weak reflector and in the second model, a strong one. The monitor models differ from the baseline models in both experiments by a 5% velocity perturbation in a rectangular lens of 400 m width within the 4^{th} layer. The density was considered constant in all models (2200 kg/m^3). We used 2 passes of a 20-point triangular moving-average filter on the baseline models to create the corresponding background models. The singular models are the differences between the complete and background models.

In this study we consider both the background and singular parts of the baseline velocity model as fully known.

The numerical experiments consisted of the following basic steps:

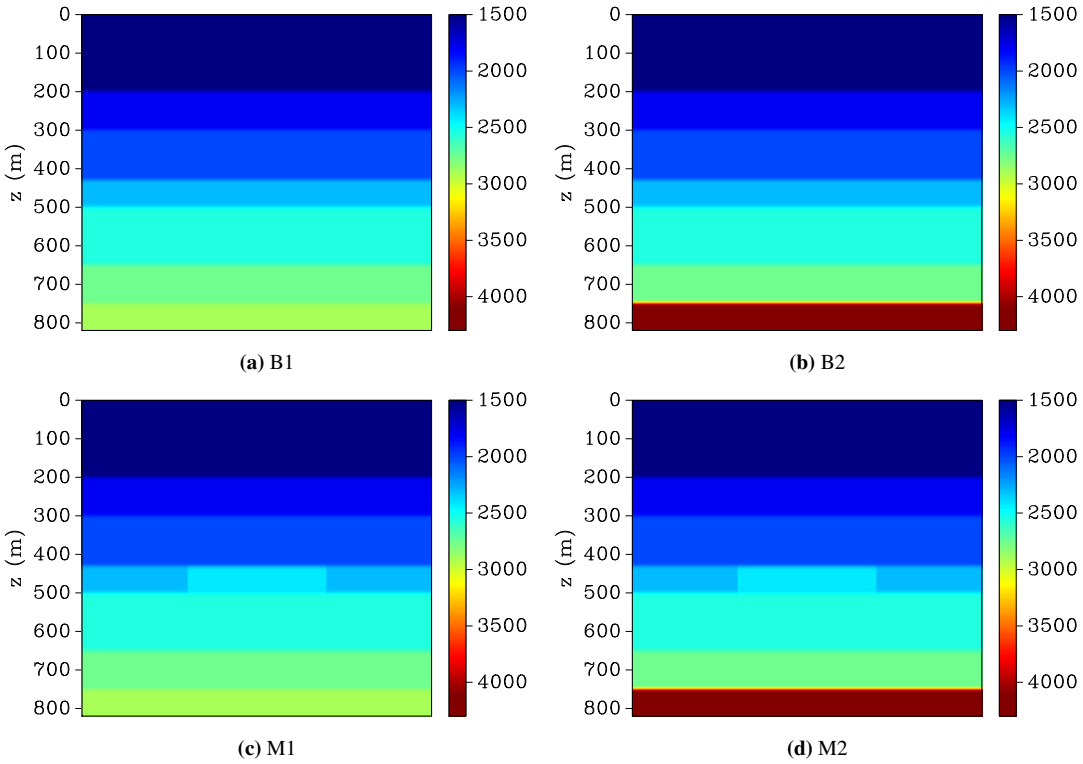

(a) B1 **(b)** B2

(c) M1 **(d)** M2

Figure 3: Center parts of the baseline (a and b) and monitor (c and d) models for model sets 1 (a and c) and 2 (b and d).

1. Simulation of the seismic acquisition by modeling the wavefields in the baseline and monitor models.
2. Computation of the true scattered-wavefield residual, which in this case is identical to the true full-wavefield residual, i.e., the difference between the wavefields in the monitor and baseline models.
3. Modeling the wavefield in the smooth background model.
4. Computation of the scattered wavefield, i.e., the difference between the wavefields in the baseline and background models.
5. Backpropagation of the true scattered-wavefield residual using the receiver-side reference and scattered wavefields.
6. Determination of the four contributions to equation (5) by crosscorrelation of the backpropagated wavefield residual with the source-side reference and scattered wavefields as exemplified in equation (4).
7. Stack of the resulting contributions over sources and receivers.

Large offset surveys

The first acquisition geometry consisted of 87 shot gather with 726 receivers each, placed at 10 m depth, spaced at 4 m, and covering the distance between 0 m and 2900 m. Sources were placed at 40 m depth spaced at 32 m, and covering the distance between 80 m and 2832 m earth's surface, Thus, the survey was positined almost symmetrically over the rectangular perturbation, centered at 1500 m. Figure 4 indicates the source positions by black stars and every 10th receiver position by a downward-pointing triangle.

In Figure 4a, we show the estimate for the singular-part bulk-modulus perturbation in model set 1 with all four contributions according to equation (5). For comparison, Figure 4b shows the corresponding

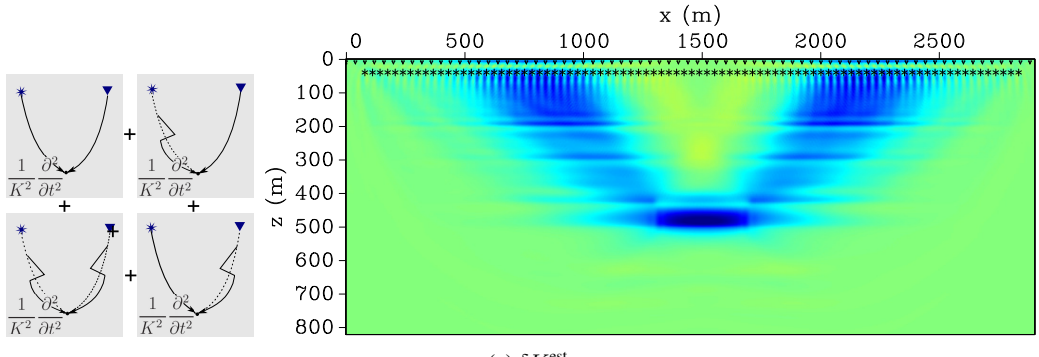

(a) δK_S^{est}

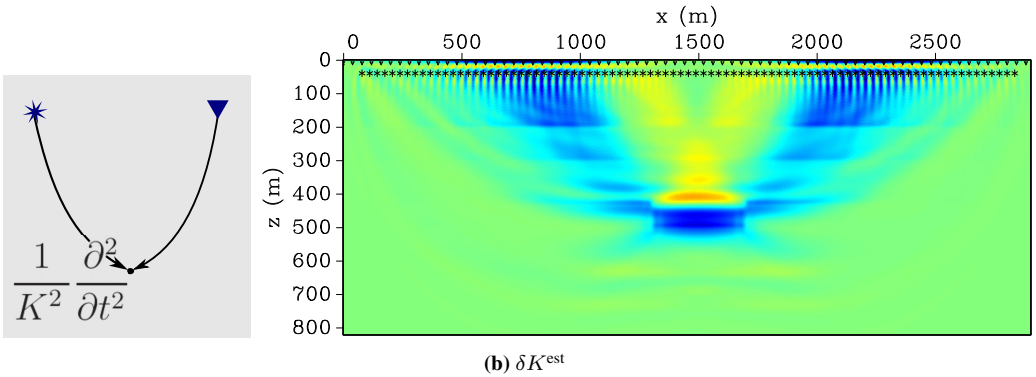

(b) δK^{est}

Figure 4: Estimates for bulk-modulus perturbation for model set 1 without a strong reflector. (a) Singular part estimate according to equation (5); (b) Conventional perturbation estimate using wave propagation in the background model. Corresponds to contribution $\delta K^{\text{est}}_{S,0\text{S}0}$.

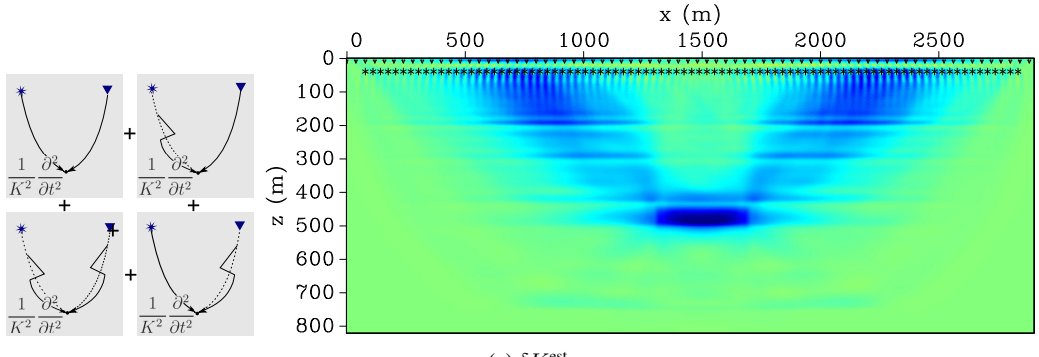

(a) δK_S^{est}

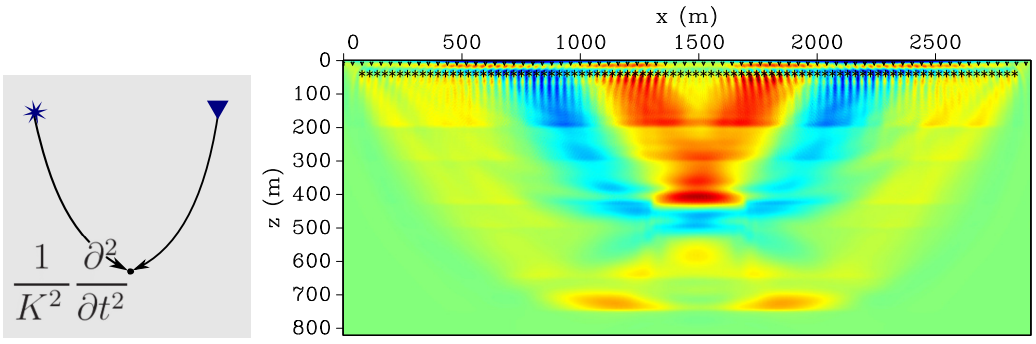

(b) δK^{est}

Figure 5: Estimates for bulk-modulus perturbation for model set 2 with a strong reflector. (a) Singular part estimate according to equation (5); (b) Conventional perturbation estimate using wave propagation in the background model. Corresponds to contribution $\delta K^{\text{est}}_{S,0\text{S}0}$.

estimate from the single-scattering contribution only. Note that this is the result that would be obtained from conventional inversion with a smoothed background model. We see that in the absence of a strong reflector in the bottom of the model, the conventional sensitivity kernel gives a satisfactory estimate.

The corresponding results for model set 2 with the strong bottom reflector are depicted in Figure 5. While the estimate from all contributions (Figure 5a) together looks similar to the one in Figure 4a, the conventional estimate is visibly different (see Figure 5b), indicating that in this situation, the use of a smooth background model to simulate the backpropagation is insufficient. We conclude that in this case, multiple-scattering contributions carry important information that cannot be neglected. We may think of the scatterers contributing to the inversion by self-illumination.

In Figure 6 we exhibit the individual contributions to δK_S^{est} of Figure 5(a) for model set 2. We see that particularly the contributions using the scattered wavefield at one side of the propagation carry important information on the position of the medium perturbation. Note that the last contribution (Figure 6d) has a signficantly lower magnitude than the other three.

Narrow offset surveys

It is known in the literature on FWI that the acquisition geometry has a strong influence on the inversion result. When inversion is done with enclosing, source and receiver arrays behave as in transmission tomography, which is known to recover very well the low-frequency information (see,e.g., Pratt, 1999; Brenders and Pratt, 2007). On the other hand, according to Zhu et al. (2009), when dealing with reflection/scattered data, narrower offsets (or reflection angles) may lead to fast-varying sensitivity kernels, in opposition to slow-varying ones in large-offset acquisitions. Fast-varying sensitivity kernels cause slower convergence of the inversion procedure.

To investigate this effect in the case of the decomposed inversion, we repeated the above experiments with a shorter survey. The new acquisition geometry consisted of 48 shot gather with 251 receivers each, and covering the distance between 0 m and 1000 m. Sources were spaced at 20 m and covering the distance between 48 m and 948 m earth's surface, Thus, the survey was positined almost symmetrically over the rectangular perturbation, now centered at 500 m. All other parameters were the same as in the first survey. Figure 7 indicates the source positions by black stars and every 10th receiver position by a downward-pointing triangle.

Figures 7(a) and 8(a) show the short-offset estimate for the singular-part bulk-modulus perturbation in both model sets with all four contributions according to equation (5), and Figures 7(b) and 8(b) depict the corresponding conventional estimates. As expected, the figures display fast-varying estimates due to the narrow-offset illumination. As for the long-offset survey, the conventional estimate is rather similar to the four-contributions estimate when no strong reflector is present (Figure 7), but visibly worse with the strong reflector present (Figure 7). Actually, in the latter case the four-contributions estimate is the best one, clearly indicating the importance of self-illumination. The multiple-scattered information improves the perturbation estimates, giving a less varying and more delineated response (compare Figure 8(b) with 8(a)). This indicates that the multiple-scattering contribution perceives both the low- and high-frequency content of the perturbation.

This can be understood with the help of Figure 8(c), which shows the contribution to the full estimate calculated with the source-side scattered wavefield. We see that this contribution alone does a better job then the conventional estimate of Figure 8(b), nicely delineating the top and bottom of the medium perturbation. The reason is that in this case not the source array alone, but also the singularities contribuite to the source-side wavefield in the kernel. Physically, this can be interpreted as the strong reflector illuminating the time-lapse change from bottom to top.

This short-offset experiment demonstrates that it is even more important than for long surveys to include the singular part into the model used for backpropagation, since it enhances the self-illumination due to scattering and leads to better perturbation estimates.

CONCLUSIONS

In this work we have applied the scattering decomposition of the sensitivity kernels of Macedo et al. (2011, 2012b) to the time-lapse problem, considering the time-lapse change as a perturbation of the singular part of

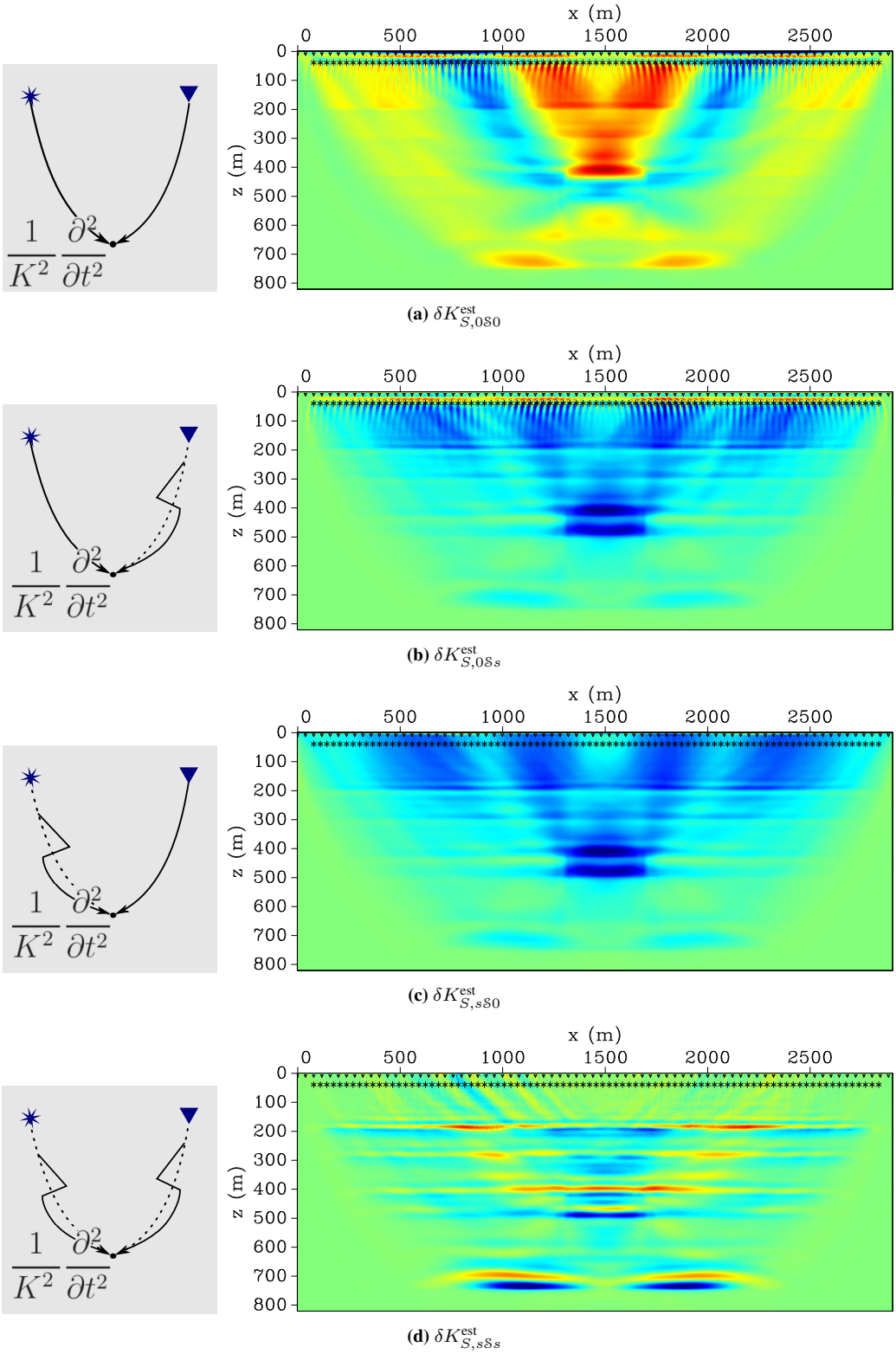

(a) $\delta K^{\text{est}}_{S,0\delta 0}$

(b) $\delta K^{\text{est}}_{S,0\delta s}$

(c) $\delta K^{\text{est}}_{S,s\delta 0}$

(d) $\delta K^{\text{est}}_{S,s\delta s}$

Figure 6: Individual contributions to δK^{est}_S for model set 2.

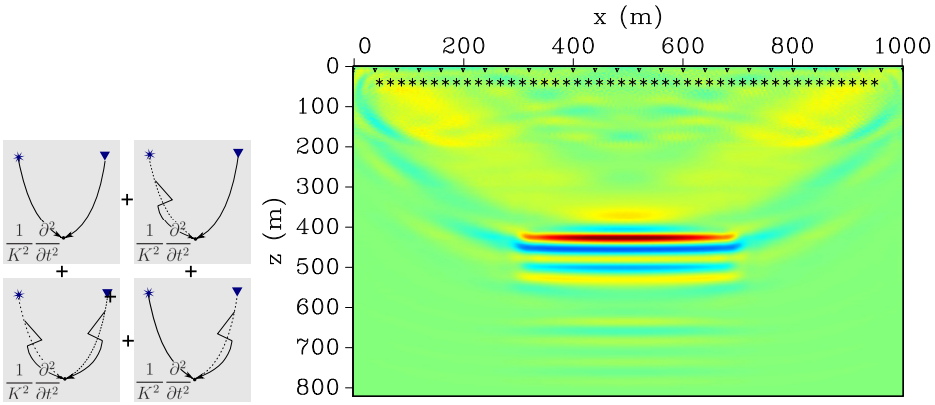

(a) δK_S^{est}

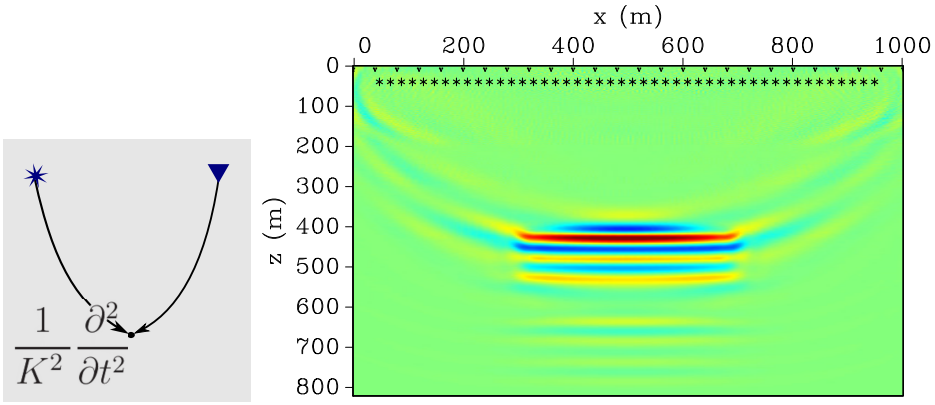

(b) δK^{est}

Figure 7: Short-offset estimates of the perturbation for model set 1 without a strong reflector. (a) Full estimate with all contributions; (b) conventional estimate, i.e., single-scattering contribution.

the model, i.e., perturbation of the scattering potential. Under the differential-method framework, we have demonstrated that the scattering-based decomposition of the sensitivity kernels allows to take advantage of the illumination of the time-lapse change due to multiple-scattering phenomena in order to improve the perturbation estimates from FWI.

We employed the FWI differential method. By considering the baseline model fully known, the data difference between baseline and monitor surveys is the residual to be minimized in order to obtain time-lapse change estimates using the baseline as starting model. Considering time-lapse change as a perturbation of only the singular part of the model, we circumvented the problem of separating the reference wavefield from the scattered field.

Our numerical experiments demonstrated that it is beneficial to include the singular part into the model used for the necessary back propagations. In the presence of a strong reflector below the time-lapse change, the use of the multiple-scattering-based sensitivity kernels yielded better estimates in both large- and narrow-offset surveys compared to estimates obtained with the conventional sensitivity kernel. In the large-offset case, it better handled the backscattered information coming from the deep reflector which would, otherwise, give rise to spurious estimates. In the narrow-offset case, the scattering-based sensitivity kernels help to bring out the low-frequency spacial information carried by the back-scattered wavefield coming up from the deep reflector. In other words, in the subkernels (e.g., $U_{S,s\mathcal{B}0}$) where the scattered wavefield acts as source-side wavefield, the singularities or reflectors that originate the scattered wavefield act as sources of illumination, enhancing and broadening the spatial spectral content of the estimate.

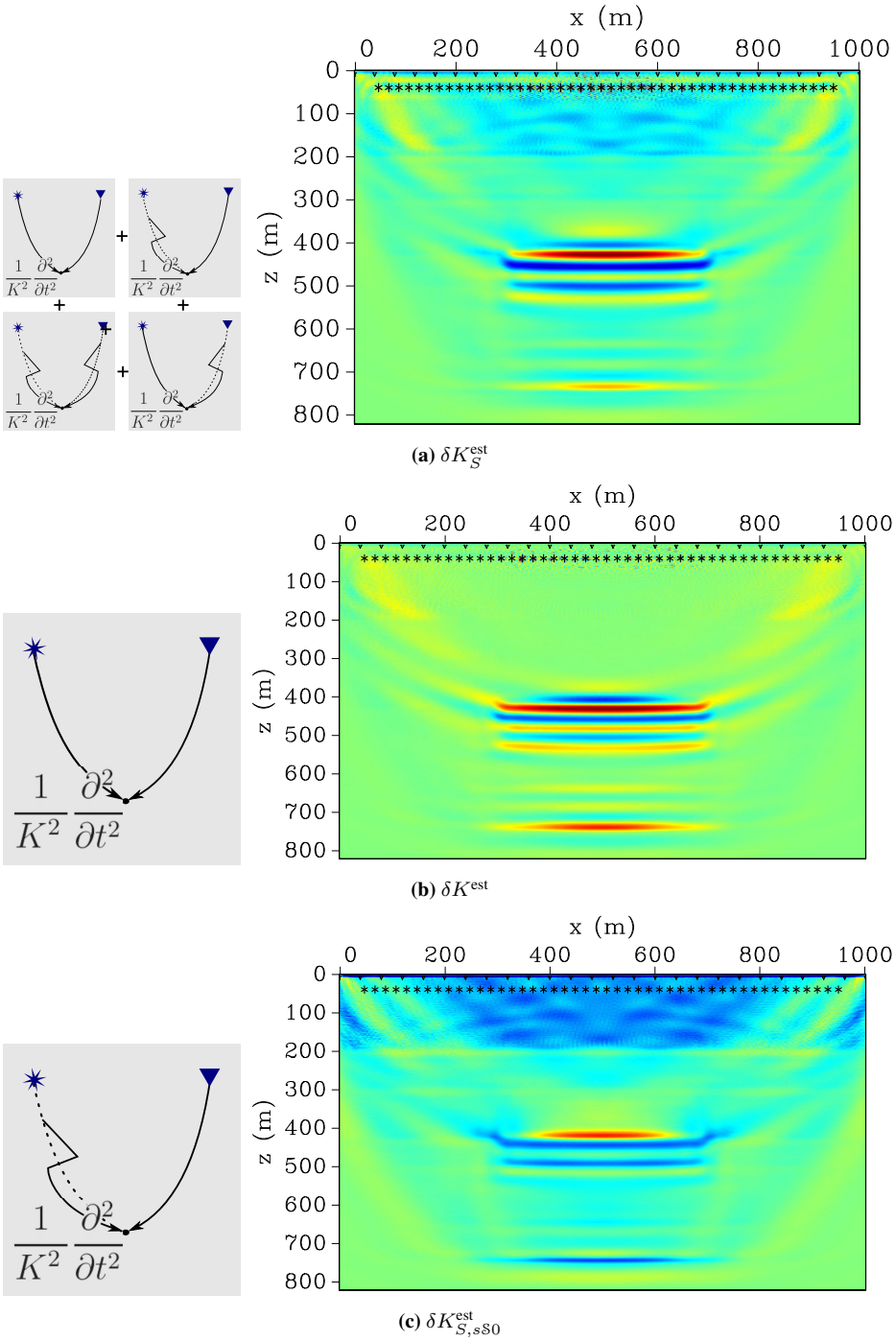

(a) δK_S^{est}

(b) δK^{est}

(c) $\delta K_{S,s80}^{\text{est}}$

Figure 8: Short-offset estimates of the perturbation for model set 2 with a strong reflector. (a) Full estimate with all contributions; (b) conventional estimate, i.e., single-scattering contribution; (c) source-side scattered-field contribution.

ACKNOWLEDGEMENTS

This work was kindly supported by the Brazilian National Research Council CNPq as well as Petrobras, Schlumberger, and the sponsors of the Wave Inversion Technology (WIT) Consortium.

REFERENCES

Asnaashari, A., Brossier, R., Garambois, S., Audebert, F., Thore, P., and Virieux, J. (2012). Time-lapse imaging using regularized FWI: a robustness study. *SEG Technical Program Expanded Abstracts*.

Brenders, A. J. and Pratt, R. G. (2007). Efficient waveform tomography for lithospheric imaging: implications for realistic, two-dimensional acquisition geometries and low-frequency data. *Geophysical Journal International*, 168(1):152–170.

Lumley, D. E. (2001). Time-lapse seismic reservoir monitoring. *Geophysics*, 66(1):50–53.

Macedo, D. L., Vasconcelos, I., and Schleicher, J. (2011). Scattering-based decomposition of sensitivity kernels for full waveform inversion. *Annual WIT report*, 15:247–260.

Macedo, D. L., Vasconcelos, I., and Schleicher, J. (2012a). A Scattering-based Reparameterization of Sensitivity Kernels for Full-waveform Inversion. *74th EAGE Conference Tecnical Program Extended Abstracts*.

Macedo, D. L., Vasconcelos, I., and Schleicher, J. (2012b). Scattering-based decomposition of sensitivity kernels for full waveform inversion – part 2: Perturbation estimates with adjoint kernels. *Annual WIT report*, 16:189–202.

Macedo, D. L., Vasconcelos, I., and Schleicher, J. (2013). Scattering-based sensitivity kernels for full-waveform inversion: taking advantage of medium self-illumination. *SEG Workshop - Full Waveform Inversion: From Near Surface to Deep*.

Plessix, R.-E., Michelet, S., Rynja, H., Kuehl, H., de Maag, J. W., and Hatchell, P. (2010). Some 3D applications of full waveform inversion. *72nd EAGE Conference Extended Abstracts*.

Pratt, R. G. (1999). Seismic waveform inversion in the frequency domain, Part 1: Theory and verification in a physical scale model. *Geophysics*, 64(3):888–901.

Queißer, M. and Singh, S. C. (2013). Full waveform inversion in the time lapse mode applied to co2 storage at sleipner. *Geophysical Prospecting*, 61(3):537–555.

Snieder, R., Grêt, A., Douma, H., and Scales, J. (2002). Coda wave interferometry for estimating nonlinear behavior in seismic velocity. *Science*, 295:2253.

Tarantola, A. (1984). Inversion of seismic reflection data in the acoustic approximation. *Geophysics*, 49(8):1259–1266.

Virieux, J. and Operto, S. (2009). An overview of full-waveform inversion in exploration geophysics. *Geophysics*, 74(6):WCC1.

Watanabe, T., Shimizu, S., Asakawa, E., and Matsuoka, T. (2004). Differential waveform tomography for time-lapse crosswell seismic data with application to gas hydrate production monitoring. *SEG Technical Program Expanded Abstracts*, (October):1–4.

Yang, D., Fehler, M., Malcolm, A., and Huang, L. (2011). Carbon sequestration monitoring with acoustic double-difference waveform inversion: A case study on sacroc walkaway vsp data. *SEG Technical Program Expanded Abstracts*, 30(1):4273–4277.

Zheng, Y., Barton, P., and Singh, S. (2011). Strategies for elastic full waveform inversion of time-lapse ocean bottom cable obc seismic data. *SEG Technical Program Expanded Abstracts*, 30(1):4195–4200.

Zhu, H., Luo, Y., Nissen-Meyer, T., Morency, C., and Tromp, J. (2009). Elastic imaging and time-lapse migration based on adjoint methods. *Geophysics*, 74(6):WCA167.